

Collective degrees of freedom of neutron-rich $A \approx 100$ nuclei and the first mass measurement of the short-lived nuclide ^{100}Rb

V. Manea,^{1,*} D. Atanasov,² D. Beck,³ K. Blaum,² C. Borgmann,² R. B. Cakirli,^{2,†} T. Eronen,² S. George,² F. Herfurth,³ A. Herlert,⁴ M. Kowalska,⁵ S. Kreim,^{2,5} Yu. A. Litvinov,³ D. Lunney,¹ D. Neidherr,³ M. Rosenbusch,⁶ L. Schweikhard,⁶ F. Wienholtz,⁶ R. N. Wolf,⁶ and K. Zuber⁷

¹CSNSM-IN2P3-CNRS, Université Paris-Sud, 91406 Orsay, France

²Max-Planck-Institut für Kernphysik, Saupfercheckweg 1, 69117 Heidelberg, Germany

³GSI Helmholtzzentrum für Schwerionenforschung GmbH, 64291 Darmstadt, Germany

⁴FAIR GmbH, 64291 Darmstadt, Germany

⁵CERN, 1211 Geneva, Switzerland

⁶Ernst-Moritz-Arndt-Universität, Institut für Physik, 17487 Greifswald, Germany

⁷Technische Universität Dresden, 01069 Dresden, Germany

(Received 1 September 2013; published 25 November 2013)

The mass surface in the $A \sim 100$ region of the nuclear chart is extended by the measurement of the $^{98-100}\text{Rb}$ isotopes with the Penning-trap mass spectrometer ISOLTRAP at ISOLDE/CERN. The mass of ^{100}Rb is determined for the first time. The studied nuclides mark the known low- Z frontier of the shape transition at $N = 60$. To describe the shape evolution towards the krypton isotopic chain, a theoretical analysis is presented in the framework of the Hartree-Fock-Bogoliubov approach. The importance of the pairing interaction for describing the extent and strength of the region of quadrupole deformation is emphasized. A later transition to large prolate deformation or, alternatively, the predominance of oblate deformation is proposed as explanation for the different behavior of the krypton isotopes. Octupole collectivity is explored as a possible mechanism for the evolution of two-neutron separation energies around $N = 56$.

DOI: [10.1103/PhysRevC.88.054322](https://doi.org/10.1103/PhysRevC.88.054322)

PACS number(s): 32.10.Bi, 82.80.Qx, 21.10.Dr, 21.60.Jz

I. INTRODUCTION

Changes in nuclear structure in the neutron-rich region of the nuclear chart around $A = 100$ are reflected in a wide range of experimental observables. Mean-square charge radii and nuclear moments, extracted from isotope-shift and hyperfine-structure measurements by laser spectroscopy, show a sudden increase at $N = 60$ in the isotopic chains above krypton ($Z = 36$) and below molybdenum ($Z = 42$) [1–6]. The energies of the first 2^+ excited states in the even-even nuclides of the region show a sudden drop at $N = 60$ in the strontium ($Z = 38$), zirconium ($Z = 40$), and molybdenum ($Z = 42$) isotopic chains [7]. The correlation of the two pictures [8] suggests the sudden onset of quadrupole deformation at $N = 60$. In the mass surface, this is observed by the increase in two-neutron separation energy between $N = 59$ and $N = 60$, qualitatively understood by the fact that the $N = 60$ isotones gain extra binding through deformation. The ratios between the energies of the first 4^+ and the first 2^+ excited states (the so-called $R_{4/2}$ ratios) of the isotopes with $N > 60$ in the deformation region come close to the condition of the rigid rotor ($R_{4/2} = 3.33$), suggesting the static character of the quadrupole deformation.

The lower border of this region of deformation has been the subject of recent debate in the literature. Despite claims that the nucleus ^{96}Kr might be deformed, based on an assumed energy of the first 2^+ excited state of only 241 keV [9], evidence from

Coulomb-excitation spectroscopy [10] and mass spectrometry [11] supports the fact that ^{96}Kr is almost spherical. This conclusion is consistent with charge-radii results [1].

On the one hand, the possibility of sudden structural changes in unexplored regions of the nuclear chart challenges our theoretical understanding of the atomic nucleus. On the other hand, various nucleosynthesis processes involve nuclei in such exotic regions. Their description requires input nuclear properties such as the β -decay half-lives or binding energies. Many of the needed nuclei, however, remain inaccessible at present radioactive beam facilities and their properties have to be obtained from model calculations. In the neutron-rich $A \sim 100$ region, sudden changes in the mass surface make extrapolations hazardous [12] and alter the predicted natural abundance of the elements [13].

The neutron-rich $A \sim 100$ region has thus been extensively studied theoretically, in order to associate the pronounced signatures in the experimental observables with structural changes in the single-particle or collective nuclear degrees of freedom. Models agree that the neutron-rich $A \sim 100$ nuclei undergo a nuclear-state transition with the addition of neutrons between the $N = 50$ and $N = 82$ shells. In the single-particle picture, this is represented by the fact that the ground state of the nuclei in the region changes from a pure to a mixed configuration of spherical single-particle states. In the macroscopic picture, this translates into a change of the nuclear shape from spherical to deformed, which signals a breaking of the rotational symmetry. Both pictures come together in the quantum Jahn-Teller effect of spontaneous symmetry breaking [14], in which the nuclear ground state can acquire a symmetry-breaking shape as a consequence of the coupling

*vladimir.manea@cern.ch

[†]Present address: Department of Physics, University of Istanbul, Istanbul, Turkey

between degenerate single-particle states and collective modes of the nucleus. The analogy between the resulting nuclear shapes, or the coexistence and transition between them, and quantum phases, has led to the description of shape-evolution in the formalism of quantum phase transitions (for a recent review, see [15]).

The role of the residual proton-neutron interaction to produce the systematics of experimental observables in the neutron-rich $A \sim 100$ region was recognized in early shell-model calculations [16,17], especially the interaction between protons and neutrons occupying orbits with large spatial overlap, as emphasized by Federman and Pittel [16]. In this picture, the quantitative aspects of the onset of quadrupole deformation are the result of the fine balance between the pairing interaction, which favours spherical shapes, and the p - n interaction, which drives collectivity and hence deformation.

Theoretical approaches such as the interacting boson model (IBM) [18] and Hartree-Fock-Bogoliubov (HFB) [19,20] are widespread approaches to illustrate the onset of collectivity and its consequences on the nuclear observables. The intrinsic-state formalism is used to reconcile the symmetry-breaking concept of nuclear deformation with the requirement of describing the nuclear ground state by eigenfunctions of the total angular momentum. It also allows for going beyond the static picture of deformation by including the effects of dynamic correlations on the ground-state energy. Calculations using the HFB formalism and the Gogny interaction [19,20] describe the systematics of two-neutron separation energies and charge radii in the region as the result of quadrupole deformation. The results show the fine interplay between oblate and prolate shapes in the region, in some cases almost degenerate in energy, as well as the role of triaxiality. HFB calculations using the Skyrme SLy4 interaction [21] and including configuration mixing by the generator coordinate method (GCM) [22] also predict the onset of quadrupole deformation, although earlier than observed experimentally.

In this work we report the determination of the masses of $^{98-100}\text{Rb}$ with the Penning-trap mass spectrometer ISOLTRAP at ISOLDE/CERN [23]. The paper is organized as follows. In Sec. II we present the ISOLTRAP setup and the results of the rubidium mass-spectrometry experiment. In Sec. III A we compare the systematics of two-neutron separation energies and charge radii in the region with the results of HFB calculations, aimed at connecting the distinctive features of the experimental observables to the underlying nuclear structure, both from the macroscopic (shape) and single-particle points of view. The changes between the rubidium and krypton isotopic chains are discussed. In Sec. III B we extend our analysis to the $N \sim 56$ region and investigate the role of dynamic octupole correlations in explaining the global picture of the mass surface around $A = 100$.

II. EXPERIMENT

The rubidium isotopes measured in this work were produced by the ISOLDE radioactive ion-beam facility [23] at CERN, as fission products from the reaction between a 1.4-GeV proton beam and a thick uranium carbide target. The initially neutral fission products were extracted from the hot

target (ca. 1800 °C) by the processes of thermal effusion and diffusion, then surface ionized in a heated (ca. 1800–2000 °C) tantalum cavity. The obtained flux of singly charged ions was accelerated to a kinetic energy of 50 keV and transported through the ISOLDE high-resolution separator (HRS). The continuous ion beam was normally blocked by the ISOLDE beam gate, which is an electrostatic deflector connected to a TTL-controlled high-voltage switch. By switching the deflection voltage the beam gate was opened, i.e., the ion beam was allowed to pass through the gate only for the duration of the applied TTL control pulse. This way one could adjust the number of ions (nuclide of interest and isobaric contaminants) which were transported in a single pulse to the ISOLTRAP setup. In the case of the present experiment, due to a favourable combination of production cross-section and ionization efficiency, the rubidium beam arriving at the ISOLTRAP setup had negligible amount of isobaric contaminations.

The schematic of the ISOLTRAP experiment [24] is presented in Fig. 1 (for a recent review, see [25]). Due to the short half-life of the rubidium isotopes, the experimental cycle of the ISOLTRAP experiment was synchronized to the impact of the proton pulse on the target. After each proton pulse, the ISOLDE beam gate was opened for a certain period of time and the rubidium beam was accumulated, cooled by collisions with helium buffer gas and bunched in a linear radiofrequency quadrupole (RFQ) [26]. The resulting bunch of rubidium ions was subsequently trapped in the multireflection time-of-flight mass separator (MR-TOF MS) [27,28] and the preparation Penning trap [29], both of which were operated with a short, low resolving-power cycle (2.5 ms and 110 ms, respectively) due to the high purity of the ISOLDE beam.

After axial cooling and mass-selective buffer-gas centering cycle [30] in the preparation Penning trap, the rubidium ions were transported to the precision Penning trap, where their cyclotron frequency was measured by the time-of-flight ion-cyclotron-resonance (TOF-ICR) technique [31]. The cyclotron frequency ν_c of an ion is connected to its mass m_i by

$$\nu_c = \frac{1}{2\pi} \frac{qB}{m_i}, \quad (1)$$

where q is the ion's charge and B is the magnetic-field strength. Since the rubidium ions were singly charged, q is equal to the elementary charge and $m_i = m_a - m_e$, with m_a the atomic mass of the species of interest and m_e the electron mass. Measuring the cyclotron frequency of the ion of interest and of a reference ion of well-known mass (in the present case, $^{85}\text{Rb}^+$ from the off-line alkali ion source of the ISOLTRAP setup) one obtains the cyclotron-frequency ratio:

$$r = \nu_{c,\text{ref}}/\nu_c = m_i/m_{\text{ref},i}, \quad (2)$$

from which the mass of the ion of interest can be determined, with a typical relative uncertainty better than 10^{-7} . The atomic mass of the species of interest m_a is then given by

$$m_a = r(m_{\text{ref},a} - m_e) + m_e, \quad (3)$$

where $m_{\text{ref},a}$ is the atomic mass of the reference species.

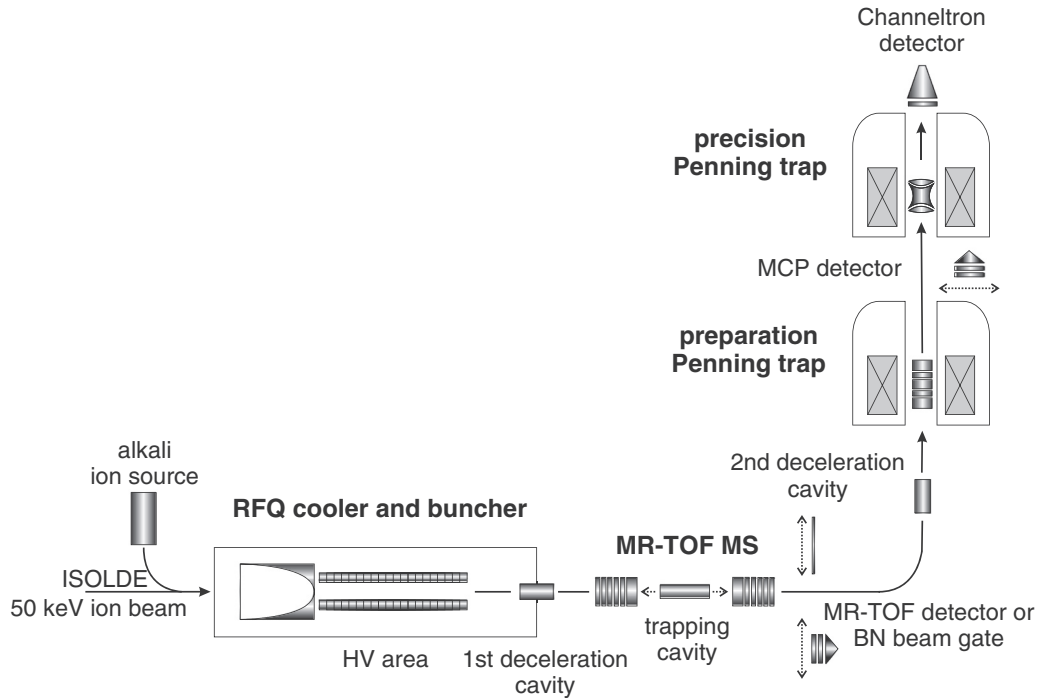


FIG. 1. Schematic view of the ISOLTRAP experiment. For details, see text.

In the present experiment we have determined the masses of $^{98-100}\text{Rb}$ (for a summary of the results see Table I). The mass of ^{100}Rb was determined for the first time. The mass of ^{99}Rb agrees with the previous value from the mass evaluation [32] (based on [33,34]), but the uncertainty was significantly reduced. The ^{98}Rb measurement provides a second frequency-ratio value, of similar uncertainty but 2σ away from the value determined in [13]. Due to the low yield and short half-life of the rubidium isotopes, the Ramsey-type TOF-ICR method [36,37] was used to measure the cyclotron frequencies of $^{99,100}\text{Rb}^+$, ensuring a lower statistical uncertainty than the conventional TOF-ICR for the same number of events and excitation time. Figure 2 presents a Ramsey-type TOF-ICR spectrum of $^{100}\text{Rb}^+$. With this measurement, ^{100}Rb becomes the shortest-lived nuclide measured using the ISOLTRAP Penning-trap mass spectrometer (half-life of 48(3) ms, according to NUBASE2012 [35]). In the case of ^{98}Rb , we have performed conventional TOF-ICR measurements, in order to look for the possible presence of an isomeric state, recently sought after but not observed during a Penning-trap experiment at TITAN [13]. However, the ^{98}Rb isomeric state was also not observed during our experiment.

III. DISCUSSION

A. Quadrupole deformation around $N = 60$

As shown in Fig. 3, the masses of the measured rubidium isotopes, together with the known charge radii [2], suggest that the sudden shape transition at $N = 60$ extends at least as far as $Z = 37$, while for $Z = 36$ the measured masses [11] and radii [1] suggest that no such shape transition takes place for ^{96}Kr . This latter conclusion is supported by the recently proposed energy of the first 2^+ excited state in ^{96}Kr [10]. Nevertheless, the available experimental data do not rule out the possibility that the shape transition is still present in the krypton isotopic chain, but shifted to higher neutron numbers.

Therefore, in order to investigate the shape evolution in the $A \sim 100$ region of the nuclear chart, we have performed Hartree-Fock-Bogoliubov (HFB) calculations [38] in the isotopic chains between krypton and zirconium, using the symmetry-unconstrained HFODD code [39] and the SLy4 interaction [21]. A contact volume-pairing force was used. The HFODD solver uses the expansion of the wave function in a harmonic-oscillator (HO) basis. Due to the arbitrariness of choosing a specific shape for the HO generating the basis,

TABLE I. Frequency ratios and mass excess (ME) values of the rubidium isotopes measured in this work. The half-lives of the isotopes from NUBASE2012 [35] and the mass excess values from AME2012 [32] are also given (# indicates extrapolated values). The last column specifies the references contributing to the AME2012.

Isotope	Half-life (ms)	$r = \nu_{c,\text{ref}}/\nu_c$	ME_{ISOLTRAP} (keV)	ME_{AME2012} (keV)	Refs.
^{98}Rb	114(5)	1.153453259(51)	-54309.4(4.0)	-54318(3)	[13]
^{99}Rb	54(4)	1.165270584(57)	-51120.3(4.5)	-51210(110)	[33,34]
^{100}Rb	48(3)	1.17710920(25)	-46247(20)	-46550#(200#)	

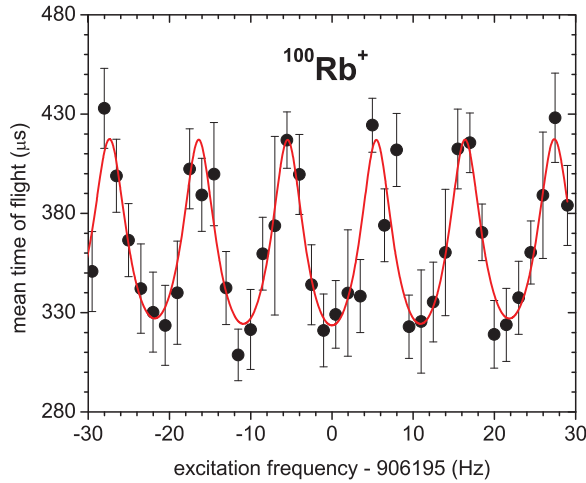


FIG. 2. (Color online) Ramsey-type time-of-flight ion-cyclotron resonance of $^{100}\text{Rb}^+$ ions with fit curve for determining the cyclotron frequency [37,41].

we used a spherical basis of maximum 300 HO functions, which proved to give satisfactory results within reasonable computational time. The broken symmetries of the calculation were chosen such that solutions with quadrupole and octupole deformation are possible. Odd- A and odd-odd nuclei were calculated in the so-called false vacuum approximation, i.e., considering the ground-state wave function as a fully paired HFB vacuum [40]. Since in this work we are only interested in describing two-neutron separation energies and charge radii, not the odd-even staggering phenomenon or the empirical pairing gap, we consider this approximation suitable. An extension of the present calculations would be to treat odd- A and odd-odd nuclei in the blocking approximation.

A spherical solution to the HFB problem was obtained by constraining the leading (dipole, quadrupole and octupole) moments to zero. The deformed solution was obtained by the so-called kick-off method. For each nucleus, ten HFB iterations were performed constraining the quadrupole moment to have a high (positive or negative) value, after which the rest of the iterations until convergence were left unconstrained. This significantly improved the convergence of the deformed solutions with respect to the fully constrained calculation.

In general, the effect of static deformation, as well as the effect of zero-point fluctuations (dynamic correlations) on the nuclear ground state is to provide an enhanced binding (equivalently, to lower the ground-state energy). This is not true for deformed excited states of the nucleus, which correspond to locally stable configurations at higher energy than the ground state (which can itself be deformed or spherical). In the following, we will not be referring to these latter configurations. Naming the enhanced-binding contribution ϵ_{corr} , the total ground-state energy E_{tot} can be written

$$E_{\text{tot}}(Z, N) = E_{\beta=0}(Z, N) + \epsilon_{\text{corr}}(Z, N), \quad (4)$$

where E and ϵ are chosen as negative quantities. $E_{\beta=0}$ is the ground-state energy of the spherical nucleus. The definition of

the two-neutron separation energy S_{2N} is

$$S_{2N}(Z, N) = E_{\text{tot}}(Z, N-2) - E_{\text{tot}}(Z, N) \equiv \Delta_{2N}[E_{\text{tot}}(N)], \quad (5)$$

where we have named the above algebraic operation (mass filter) Δ_{2N} . To emphasize the effect of correlations on the two-neutron separation energy, we need to calculate S_{2N} from Eq. (4):

$$\begin{aligned} S_{2N}(Z, N) &= \Delta_{2N}[E_{\beta=0}(Z, N) + \epsilon_{\text{corr}}(Z, N)] \\ &= S_{2N, \beta=0}(Z, N) + \Delta_{2N}[\epsilon_{\text{corr}}(Z, N)], \end{aligned} \quad (6)$$

which shows that the two-neutron separation energy is the sum of the value in the absence of correlations/deformation and the derivative (in the sense of Δ_{2N}) of the correlation/deformation energy.

The nuclear charge radii (plotted as $\delta\langle r^2 \rangle_{N,50} = \langle r^2 \rangle_N - \langle r^2 \rangle_{N=50}$) and two-neutron separation energies resulting from our HFB calculations are compared in Fig. 3 to the available experimental data from the literature and this work, for different values of the proton (V_π) and neutron (V_ν) pairing interactions. We pay special attention to the pairing force due to its essential role in the Federman-Pittel mechanism of deformation, proposed in [16] for explaining the onset of deformation at $N = 60$ in the zirconium isotopic chain. In the Federman-Pittel mechanism, the main driving force for configuration mixing and collectivity is the residual interaction between protons and neutrons in orbits with large spatial overlap. The effect of the n - n and p - p pairing interaction is opposite, favoring a spherical shape of the nucleus. Following Ref. [16], the competition between the two contrary forces is what determines the fine details of the evolution of collectivity with the addition of protons and neutrons to the nucleus. For the neutron-rich $A \sim 100$ nuclei, the spatial correlation of the $\pi g_{9/2}$ and $\nu g_{7/2}$ orbits translates into a strongly attractive p - n interaction. Filling the $\nu g_{7/2}$ orbital favors the excitation of protons to the normally unoccupied $\pi g_{9/2}$ level, leading to a phenomenon of mutual p - n polarization. Shell-model calculations including this mechanism for the zirconium isotopes predict almost pure ground-state configurations up to $N = 58$ [16]. However, the low-lying first excited 0^+ state approaches the ground state towards $N = 60$ and displays a strongly mixed configuration. At $N = 60$, the configuration of the ground state changes from pure to mixed, signaling that the intruder 0^+ state has become the ground state.

Both oblate and prolate solutions were found in our calculations, lying close in energy, in agreement with the HFB results presented in Refs. [19,20] for a Gogny-type interaction. The spherical solution is also shown in Fig. 3 to emphasize the effect of deformation in connection to Eq. (6), where it corresponds to $S_{2N, \beta=0}$. For each of the deformed solutions, only the values lower in energy than the spherical solution are shown. With ϵ_{corr} representing the difference in energy between the spherical solution and the deformed one, Eq. (6) explains the signature in the two-neutron separation energies with the onset of quadrupole deformation at $N = 60$: the increase in deformation energy is large enough at $N = 60$ [the second term in Eq. (6)], that S_{2N} is greater for $N = 60$

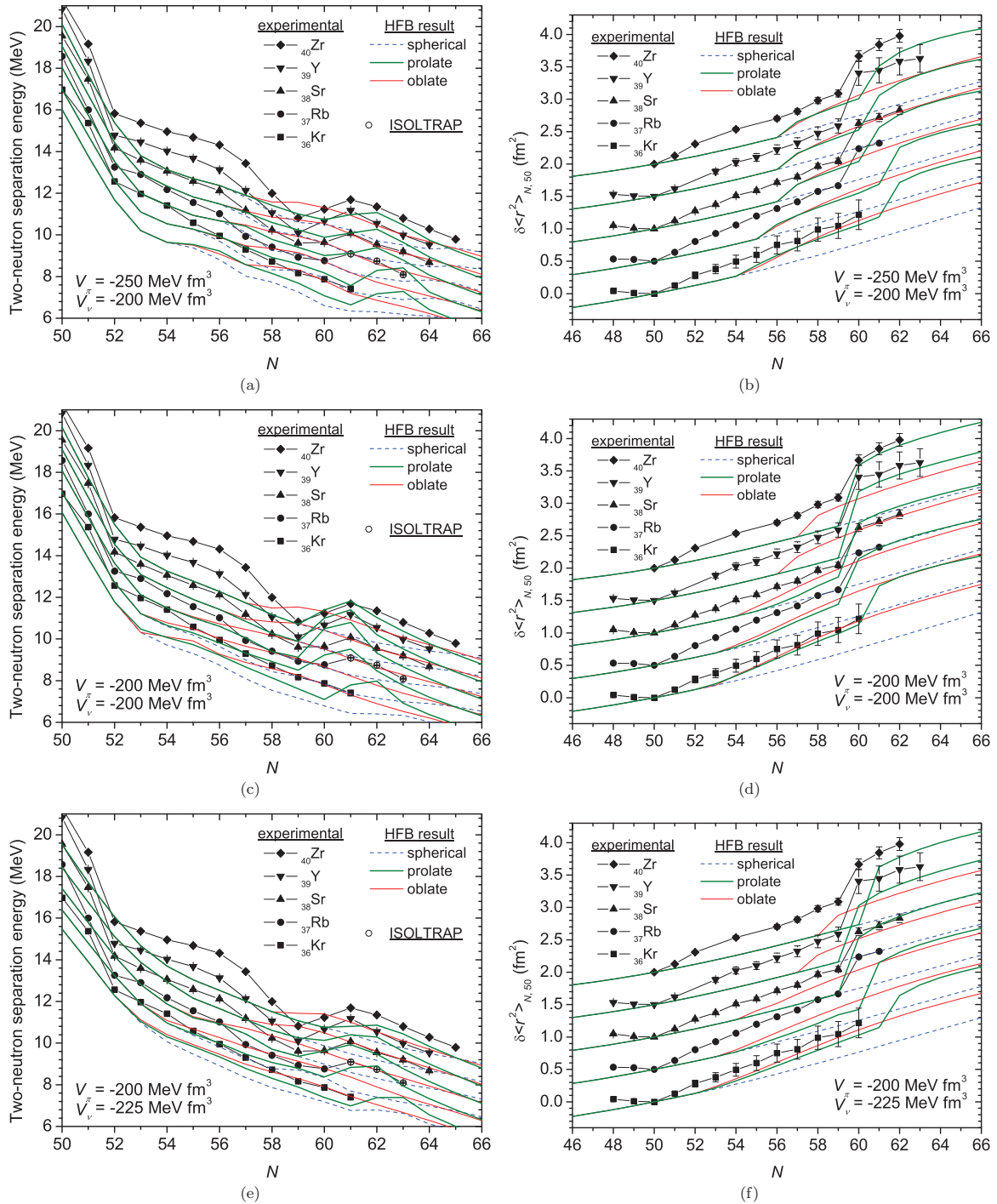


FIG. 3. (Color online) Experimental two-neutron separation energies (left column) and changes in mean-square charge radii $\delta \langle r^2 \rangle_{N,50}$ relative to the respective $N = 50$ isotopes (right column) of $A \sim 100$ nuclei [1–6,32] compared to predictions of HFB calculations with the SLy4 potential and different strengths of the proton and neutron pairing interactions. The spherical solution is shown (blue dashed line), as well as the prolate-deformed (green thick line) and the oblate-deformed (red thin line) solutions. Only the deformed solutions lower in energy than the spherical one are considered. The experimental values influenced by the reported rubidium masses are represented with open symbols. For clarity, the $\delta \langle r^2 \rangle_{N,50}$ are plotted with an arbitrary offset with respect to the krypton chain. Note that for the experimental charge radii, the uncertainty in the slope for each isotopic chain can reach several percent. However, it does not change the fine details, such as sudden changes in radii.

than for $N = 59$. In the HFB approach, the separation of Eq. (4) thus emerges naturally. One notices in Fig. 3 also the reverse effect to the enhancement of S_{2N} at $N \sim 60$: a decrease

of the correlation energy leads to values of S_{2N} lower than the corresponding spherical solution (effect observed towards $N = 66$).

The prolate solution describes best the observed systematics of two-neutron separation energies and charge radii beyond $N = 60$, irrespective of the used pairing interaction. In general, two prolate minima were found: one at lower deformation, mainly stable for $N < 60$ and one at larger deformation, emerging around $N = 60$. The green line in Fig. 3 represents the lowest-energy prolate configuration obtained, which from $N \sim 60$ onward is the strongly deformed one. Figure 3 thus shows that the shape transition at $N = 60$ can be qualitatively explained either as a change between an oblate and a prolate shape, or as the change between a low-deformation and a high-deformation prolate shape. The offset of the calculated results from the experimental values close to $N = 50$ can be explained by missing dynamic correlations, which should be included in the HFB calculation beyond the static mean field. Their effect is to produce a dynamic contribution to the nuclear charge radius and to the binding energy even when the static nuclear shape is spherical. In order to account for this contribution, the generator coordinate method (GCM) is a widespread approach for treating the mixing of the different deformed configurations [22,38] in the nuclear ground state.

The prolate-deformed single-particle picture (Nilsson levels) resulting from our calculations is presented in Fig. 4 for the rubidium isotopes between $N = 54$ and $N = 60$, using for the pairing interactions $V_\pi = V_\nu = -200 \text{ MeV fm}^3$. The spherical single-particle energies of the magic ^{87}Rb are also shown. Unlike the typical Nilsson diagrams, Fig. 4 shows the single-particle energies as a function of neutron number. As such, they are not only modified by the evolution of deformation along the isotopic chain, but also by the change of the energies of the spherical shells with the addition of neutrons. The quadrupole deformation parameter, β_2 , obtained for each of the isotopes considered, is specified on the upper abscissa of the diagrams. One notices that, when passing from $N = 59$ to $N = 60$, the rubidium isotopes exhibit a jump from moderate to pronounced quadrupole deformation.

With the increase of quadrupole deformation intruder orbits from the $\pi g_{9/2}$ and $\nu h_{11/2}$ spherical shells are gradually lowered in energy and eventually mix in the ground-state configuration. The last occupied levels of the $N = 60$ isotones are $\frac{1}{2}[4, 4, 0]$, $\frac{3}{2}[4, 3, 1]$ (for protons) and $\frac{5}{2}[4, 0, 4]$, $\frac{1}{2}[5, 5, 0]$, $\frac{3}{2}[5, 4, 1]$ (for neutrons). Together with the normally occupied orbits, they create a configuration of enhanced binding which drives the shape transition at $N = 60$, as discussed in [10,42].

In Fig. 3, one notices that the beginning of the region of deformed nuclei depends significantly on the strength of the pairing interaction. One also observes that moderate quadrupole deformation starts to set in earlier than $N = 60$, which is also in agreement with the systematics of experimental charge radii, exhibiting a small change of slope at $N = 57$ (which can be observed, for example, in the zirconium isotopic chain). A rather specific choice of the pairing interaction ($V_\pi = V_\nu = -200 \text{ MeV fm}^3$) is required to reproduce the border of the region of large deformation and the strength of the observed signatures in the experimental observables down to rubidium, including $^{98-100}\text{Rb}$ [see Figs. 3(c) and 3(d)]. With this choice one also obtains that the prolate solution, which offers the best agreement, is energetically favoured (has lower energy) for $N > 60$ with respect to the oblate

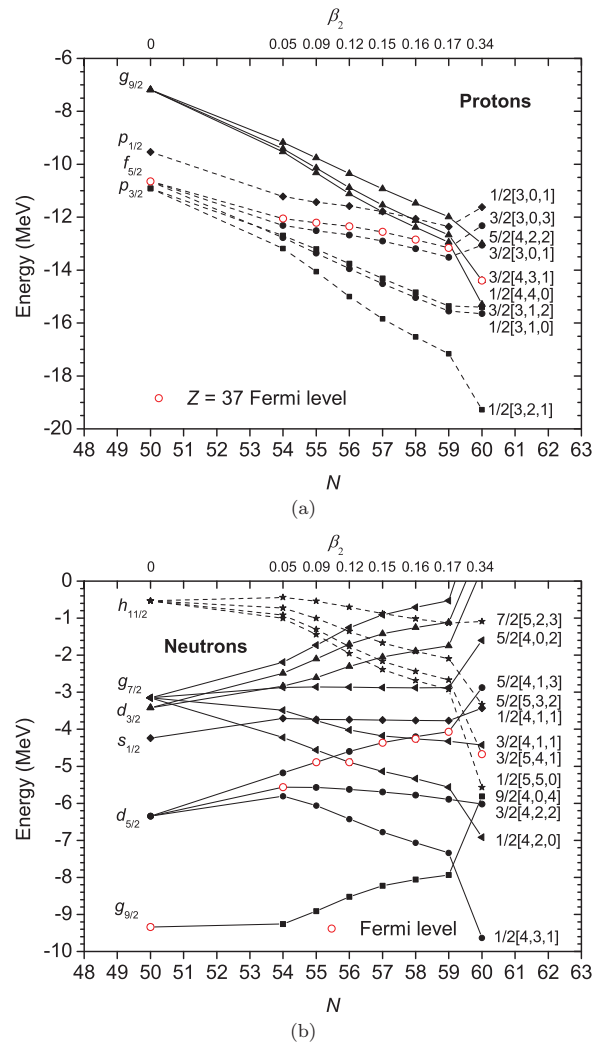


FIG. 4. (Color online) Single-particle energies of protons (upper panel) and neutrons (lower panel) in the rubidium isotopic chain, presented as a function of the neutron number for the corresponding prolate-deformed solutions. The obtained quadrupole deformation parameter β_2 is specified for each N value.

solution (as opposed, for example, to $V_\pi = -250 \text{ MeV fm}^3$, $V_\nu = -200 \text{ MeV fm}^3$, for which the oblate solution is always favored).

For this choice of pairing strength, the calculation also correctly predicts that ^{96}Kr is not in the region of strong deformation, as was shown from measurements of charge radii [1] and binding energies [11]. However, the transition between weakly deformed and strongly deformed shape is still predicted to take place in the prolate solutions of the krypton isotopes, but for higher neutron numbers ($N = 61$ and 62). The actual behavior of the ground-state observables is determined by the ordering in energy between the oblate and the prolate configurations. For $V_\pi = V_\nu = -200 \text{ MeV fm}^3$, between the rubidium and zirconium chains the oblate configuration is energetically favoured up to $N = 59$, the two configurations are almost degenerate at $N = 60$ and the strongly deformed prolate configuration is favoured for $N > 60$. In the krypton chain, the position of this equilibrium is shifted towards

$N = 62, 63$, with the two configurations remaining almost degenerate in energy for $N > 63$.

The different behavior of the two-neutron separation energies and charge radii in the krypton isotopic chain can thus be explained by a transition to the strongly deformed prolate shape after $N = 61$ (the most neutron-rich isotope measured so far), or by a persistence of the oblate shape in the nuclear ground state. Measurements of the more neutron-rich krypton isotopes (^{98}Kr and further) are thus required to clarify their shape evolution towards the neutron midshell ($N = 66$) and to establish whether the krypton chain is indeed the critical boundary of the prolate shape transition in the neutron-rich $A \sim 100$ region of the nuclear chart [11].

The results shown in Fig. 3 also underline the importance of the properties of deformed nuclei in designing precise nuclear interactions. Some of the sharp signatures in the trends of experimental observables in shape-transition regions can constitute reference observables for fitting the parameters of the nucleon-nucleon potential or the strength of the pairing interaction, which are often adjusted only to the properties of spherical nuclei [38] and to the odd-even staggering of masses [43], respectively.

B. Dynamic octupole correlations around $N = 56$

A distinctive feature of the mass surface in the here-investigated region is the drop of the two-neutron separation energies after $N = 56$ between rubidium and molybdenum, as can be partly seen from Fig. 3. The effect is maximal in the yttrium ($Z = 39$) and zirconium ($Z = 40$) isotopic chains and has been interpreted as due to the crossing of the neutron subshell $N = 56$ [11,44] (similar, but weaker, to the effect observed at the crossing of the $N = 50$ shell). This hints at an enhanced $N = 56$ subshell, which is supported by the high energy of the first 2^+ excited state in ^{96}Zr [7]. The disappearance of the kink in the two-neutron separation energies of the krypton isotopes was interpreted as a reduction of the $N = 56$ subshell gap [44].

The HFB calculations presented in Fig. 3 do not show any change in the trend of the two-neutron separation energies at $N = 56$. While the results obtained in the spherical approximation do exhibit slope changes at the filling of the neutron subshells, these weak effects are washed out, even in the most pronounced case of Fig. 3(a), by the contribution of quadrupole correlations. There is also no change of slope in the trend of the experimental charge radii corresponding to the drop of the two-neutron separation energies at $N = 56$, as is on the other hand observed for the case of $N = 50$. The g factor of the first 2^+ excited state in ^{96}Zr is consistent with the interpretation of this state being the result of the excitation of two protons across the $Z = 40$ gap, between the opposite-parity orbitals $\pi p_{1/2}$ and $\pi g_{9/2}$ [45], which underlines the closure of the $N = 56$ subshell (no neutron excitations contribute to the 2^+ state). As same-parity proton excitations become possible in the neighboring $N = 56$ isotones of ^{96}Zr , the closure of the $N = 56$ subshell no longer produces an increase of the energy of the first 2^+ state [7]. This suggests that the $N = 56$ subshell is not particularly enhanced and draws attention to the possible evolution of proton effective single-particle

energies [46]. Calculations using the IBM [18] do not predict the drop in two-neutron separation energies at $N = 56$ in the zirconium chain, but describe rather well the onset of quadrupole collectivity at $N = 60$, although the Hamiltonian is fitted to reproduce, among others, the energy of the first 2^+ excited state. This can be a sign of the necessity to define the valence space with respect to the $N = 56$ closure, or of ingredients missing from the IBM description. The evolution of nuclear structure around ^{96}Zr is not completely understood and the above observations raise the question whether the $N = 56$ subshell can by itself explain the extended effect in the two-neutron separation energies.

The nucleon (proton or neutron) number 56 is one of the numbers favoring an enhancement of octupole collectivity, due to the coupling of the opposite-parity $h_{11/2}$ and $d_{5/2}$ orbitals, which differ by three units of angular momentum [47]. The presence of octupole collectivity in the nuclides around ^{96}Zr is reflected in the existence of a 3^- level in the low-energy excitation spectrum of the even-even nuclei in the region. The transition rate from the 0^+ ground state to this 3^- level in ^{96}Zr is remarkably high [45]. The reproduction of the experimental $B(E3; 0^+ \rightarrow 3^-)$ through random-phase approximation calculations leads to its description as a collective state, dominated by the configurations $\pi(g_{9/2}) \otimes \pi(p_{3/2})^{-1}$ and $\nu(h_{11/2}) \otimes \nu(d_{5/2})^{-1}$ (excitation of a proton from the $\pi p_{3/2}$ to the $\pi g_{9/2}$ orbital and of a neutron from the $\nu d_{5/2}$ to the $\nu h_{11/2}$ orbital, respectively) [48].

The HFB calculations presented in Fig. 3 predict no static octupole deformation around $N = 56$ in any of the isotopic chains between krypton and zirconium. The predicted trends of two-neutron separation energies below $N = 58$ are rather linear and their departure from the experimental values reflects the contribution of dynamic correlations missing from the HFB calculation, which can be quadrupole, as well as octupole in nature. In Fig. 4 one notices the large gap between the $\nu d_{5/2}$ and the $\nu h_{11/2}$ shells, as well as between $\pi p_{3/2}$ and $\pi g_{9/2}$, at the level of the spherical mean field ($\beta = 0$). These large gaps make octupole vibrations unlikely in the ground-state of a spherical nucleus. Nevertheless, as was mentioned already in the previous section, the emergent quadrupole collectivity for $N > 50$ lowers the energy of intruder orbits from the $\nu h_{11/2}$ and $\pi g_{9/2}$ shells, thus reducing the effective energy gap for octupole excitations. We mention that a similar reduction of the gap takes place also for the oblate-deformed solutions, not shown in Fig. 4. For example, in the case of rubidium, the $\frac{11}{2}[4, 0, 5]$ and the $\frac{5}{2}[4, 1, 3]$ orbits, originating from the octupole-coupled ($\Delta J = 3$) neutron shells, cross already at $N \sim 57$ for the oblate-deformed solution. Quadrupole collectivity can thus dynamically provide the conditions allowing for zero-point octupole fluctuations around $N = 56$.

Returning to Eq. (6), the trends of two-neutron separation energies are sensitive to the correlation energy from zero-point quadrupole and octupole fluctuations. An increase in the absolute value of the correlation energy ($\Delta_{2N}[\epsilon_{\text{cor}}(Z, N)] > 0$) would determine a rise in the trend of S_{2N} . To illustrate that this is the case in the studied region, Fig. 5 shows the two-neutron separation energies between the krypton ($Z = 36$) and the ruthenium ($Z = 44$) isotopic chains. The red lines mark the linear trend of S_{2N} in the krypton isotopic chain, fitted between

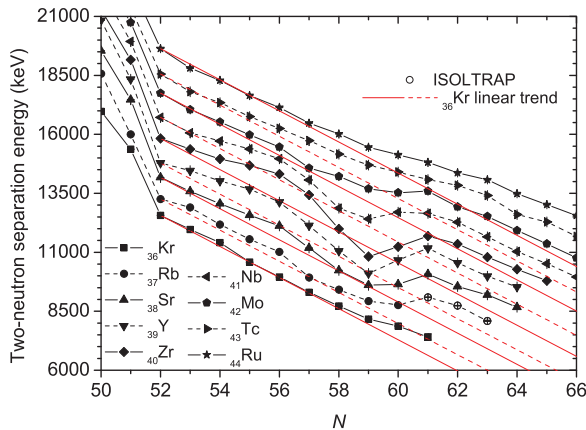


FIG. 5. (Color online) Experimental two-neutron separation energies from the literature [32] and from this work (symbols connected by lines), compared to the linear trend of the $^{88-94}\text{Kr}_{52-58}$ isotopes (straight red lines). The continuous or dashed character of the lines is chosen to facilitate comparison.

$N = 52$ and $N = 58$. The fit line is then translated to match, for each of the other isotopic chains, the S_{2N} of the $N = 52$ isotone, thus allowing for comparison. One notices that the $N = 58$ isotones fall on the same trend up to niobium ($Z = 41$), until, for larger Z , quadrupole deformation sets in already at $N = 58$. Between $N = 52$ and $N = 58$, however, the S_{2N} values show a parabolic rise above the linear trend, peaking at $N = 56$. The effect is maximum for Z between 39 and 41, but is still present for the strontium ($Z = 38$) and molybdenum ($Z = 42$) isotopes. This effect fades away for higher proton numbers and the two-neutron separation energies return in the ruthenium isotopic chain to the linear trend of the krypton isotopes.

The behavior of the two-neutron separation energies between $Z = 36$ and 44 is compatible with the gradual increase of the correlation energy in the ground state of the $N \sim 56$ isotones, peaking for $Z = 40$. The energy of the first 2^+ excited state of the $N = 56$ isotones is maximum at $Z = 40$, while the energy of the 3^- state is minimum [7], which suggests that, while quadrupole correlations are diminished for $Z = 40$, octupole collectivity is enhanced.

Hartree-Fock-Bogoliubov calculations using the Gogny D1S interaction and accounting for octupole correlations by the generator coordinate method (GCM), published in [49], also predict the nuclei in the region to have no static octupole deformation. Nevertheless, the energy of octupole vibrations around the nondeformed ground state can be significant. In the GCM formalism of [49], this dynamic octupole correlation energy can be quantified by the difference in energy between the static and the dynamic (in the sense of GCM) self-consistent solutions. The results of [49] presented in Fig. 6 show that the octupole correlation energy is enhanced for Z between 38 and 42, peaking at $Z = 40$ and $N \sim 56$. While the total predicted enhancement is not sufficient to explain the observed strength of the effect in the two-neutron separation energies, it offers a plausible explanation, alternative (or complementary) to the closure of the $N = 56$ subshell. Further refinements of the description of dynamic octupole correlations are necessary in order to clarify its impact on the mass surface around $N = 56$.

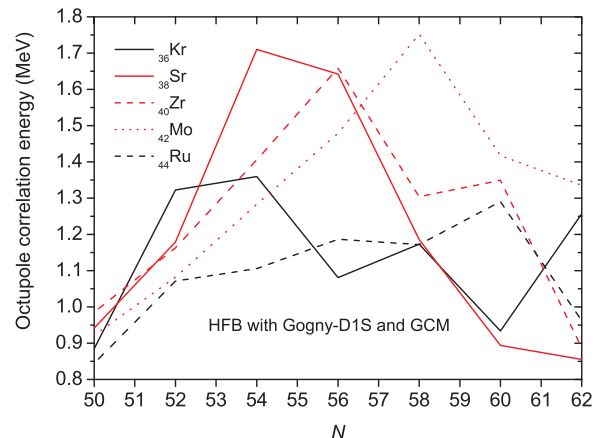


FIG. 6. (Color online) Energy of octupole correlations around $N = 56$ from HFB calculations using the Gogny-D1S potential, treated in the generator coordinate method approach [49].

IV. CONCLUSIONS AND OUTLOOK

In the present work we have reported the determination of the masses of the neutron-rich $^{98-100}\text{Rb}$ isotopes with the Penning-trap mass spectrometer ISOLTRAP at the ISOLDE/CERN facility. The mass of ^{100}Rb was determined for the first time and the mass of ^{99}Rb was significantly improved. No signs of the ^{98}Rb isomer were observed.

The measured masses confirm that the rubidium isotopes follow the trend of the isotopic chains with higher proton numbers, unlike the known krypton isotopes, for which no shape transition was found at $N = 60$ [10,11]. Thus, while $^{99,100}\text{Rb}$ are in the region of strong quadrupole deformation, the shape of their isotones $^{98,99}\text{Kr}$ is currently not known.

To understand the evolution of nuclear shapes in this region, we have performed HFB calculations with the SLy4 [21] interaction, using the HFODD code [39]. The results show that the studied nuclei exhibit a complex deformation landscape, with stable prolate and oblate configurations lying close in energy, in agreement with other HFB results from the literature [19,20]. The single-particle structure is consistent with the Federman-Pittel mechanism of nuclear collectivity [16], the driving force of which is the residual interaction between protons and neutron in orbits with large overlap, in competition with the pairing interaction, to produce the fine balance between spherical and deformed configurations.

The prolate configuration describes best the observed systematics of two-neutron separation energies and charge radii beyond $N = 60$ and down to $Z = 37$. As such, the sharp changes in the trends of experimental observables determined by the onset of quadrupole deformation pose strong constraints on the parameters of the nucleon-nucleon potential. In particular, we have shown that the pairing interaction has a significant impact on the predicted position of the shape transition, as well as the absolute values of the two-neutron separation energies and charge radii of the deformed nuclei. The ordering in energy between the prolate and the oblate configuration is also affected. This recommends the ground-state properties of nuclei in shape-transition regions as reference observables for fitting the parameters of the nuclear potential, in particular of

the pairing interaction, complementary to the commonly used properties of magic nuclei [38] and odd-even staggering of masses [43], respectively.

The HFB calculations predict that the transition to larger deformation also takes place in the prolate solution of the krypton isotopes (Fig. 3), but at higher neutron number than in the isotopic chains between rubidium and zirconium. This possibility is not excluded by the available experimental data, which only extend to $N = 61$. The oblate configuration also becomes energetically favoured with respect to the prolate one up to $N = 62$ – 63 , the two remaining almost degenerate in energy for higher neutron numbers. A prolate shape transition for higher N than the most neutron-rich krypton isotope measured so far or a persistence of the oblate configuration are both possible explanations for the different behavior of the experimental observables in the krypton isotopic chain. Measurements of more neutron-rich krypton isotopes, such as $^{98,99}\text{Kr}$, are necessary to clarify if the krypton chain is indeed the critical boundary of the prolate shape transition in the neutron-rich $A \sim 100$ region of the nuclear chart.

The lowering of intruder orbits as the result of quadrupole collectivity favours the development of dynamic octupole correlations in the $N \sim 56$ region. The drop in two-neutron separation energies at $N = 56$, previously explained as the result of the enhancement of the $N = 56$ subshell gap [44], can also be the effect of an enhancement of the energy of octupole correlations in that region, determining the increase

of S_{2N} at $N = 56$ and an apparent drop towards $N = 58$. On the S_{2N} landscape shown in Fig. 6, the $N = 59$ isotonic line would mark a valley between a hill of octupole vibrations and a plateau of static quadrupole deformation. Recent HFB calculations with the Gogny D1S interaction and the generator coordinate method [49] suggest an increase of the energy of octupole correlations around $N = 56$, supporting this picture. This reinforces the importance of dynamic correlations in the mean-field approach for describing the fine details of ground-state observables and of precise mass measurements for revealing the small effects of such correlations on the mass surface, which mean-field theory can most easily access.

ACKNOWLEDGMENTS

This work was supported by the BMBF under Contracts No. 05P12HGCI1, No. 05P12HGFNE, and No. 05P09ODCIA, the EU through ENSAR (Grant No. 262010), the French IN2P3, the ISOLDE Collaboration, and the Max-Planck Society. S.K. acknowledges support from the Robert-Bosch Foundation, R.B.C. from the Max-Planck Partner Group with MPIK, and T.E. from the Alexander von Humboldt foundation. Yu.A.L. acknowledges the Helmholtz-CAS Joint Research Group HCJRG-108. We would like to thank the ISOLDE target team for producing the rubidium beam despite exceptional technical difficulties and the ISOLDE operations team for their support.

-
- [1] M. Keim, E. Arnold, W. Borchers, U. Georg, A. Klein, R. Neugart, L. Vermeeren, R. Silverans, and P. Lievens, *Nucl. Phys. A* **586**, 219 (1995).
- [2] C. Thibault, F. Touchard, S. Büttgenbach, R. Klapisch, M. de Saint Simon, H. T. Duong, P. Jacquinet, P. Juncar, S. Liberman, P. Pillet, J. Pinard, J. L. Vialle, A. Pesnelle, and G. Huber, *Phys. Rev. C* **23**, 2720 (1981).
- [3] F. Buchinger, E. B. Ramsay, E. Arnold, W. Neu, R. Neugart, K. Wendt, R. E. Silverans, P. Lievens, L. Vermeeren, D. Berdichevsky, R. Fleming, D. W. L. Sprung, and G. Ulm, *Phys. Rev. C* **41**, 2883 (1990).
- [4] P. Lievens, R. Silverans, L. Vermeeren, W. Borchers, W. Neu, R. Neugart, K. Wendt, F. Buchinger, and E. Arnold, *Phys. Lett. B* **256**, 141 (1991).
- [5] B. Cheal, M. Gardner, M. Avgoulea, J. Billowes, M. Bissell, P. Campbell, T. Eronen, K. Flanagan, D. Forest, J. Huikari, A. Jokinen, B. Marsh, I. Moore, A. Nieminen, H. Penttil, S. Rinta-Antila, B. Tordoff, G. Tungate, and J. Äystö, *Phys. Lett. B* **645**, 133 (2007).
- [6] P. Campbell, H. L. Thayer, J. Billowes, P. Dendooven, K. T. Flanagan, D. H. Forest, J. A. R. Griffith, J. Huikari, A. Jokinen, R. Moore, A. Nieminen, G. Tungate, S. Zemlyanoi, and J. Äystö, *Phys. Rev. Lett.* **89**, 082501 (2002).
- [7] M. Bhat, in *Nuclear Data for Science and Technology*, Research Reports in Physics, edited by S. Qaim (Springer, Berlin/Heidelberg, 1992), pp. 817–821, data extracted using the NNDC On-Line Data Service from the ENSDF database (<http://www.nndc.bnl.gov>), file revised as of 30.08.2013.
- [8] R. B. Cakirli, R. F. Casten, and K. Blaum, *Phys. Rev. C* **82**, 061306(R) (2010).
- [9] N. Mărginean, D. Bucurescu, C. A. Ur, C. Mihai, L. Corradi, E. Farnea, D. Filipescu, E. Fioretto, D. Ghiță, B. Guiot, M. Górska, M. Ionescu-Bujor, A. Iordăchescu, D. Jelavić-Malenica, S. M. Lenzi, P. Mason, R. Mărginean, D. Mengoni, G. Montagnoli, D. R. Napoli, S. Pascu, G. Pollarolo, F. Recchia, A. M. Stefanini, R. Silvestri, T. Sava, F. Scarlassara, S. Szilner, and N. V. Zamfir, *Phys. Rev. C* **80**, 021301(R) (2009).
- [10] M. Albers, N. Warr, K. Nomura, A. Blazhev, J. Jolie, D. Mücher, B. Bastin, C. Bauer, C. Bernards, L. Bettermann, V. Bildstein, J. Butterworth, M. Cappellazzo, J. Cederkäll, D. Cline, I. Darby, S. Das Gupta, J. M. Daugas, T. Davinson, H. De Witte, J. Diriken, D. Filipescu, E. Fiori, C. Fransen, L. P. Gaffney, G. Georgiev, R. Gernhäuser, M. Hackstein, S. Heinze, H. Hess, M. Huysse, D. Jenkins, J. Konki, M. Kowalczyk, T. Kröll, R. Krücken, J. Litzinger, R. Lutter, N. Mărginean, C. Mihai, K. Moschner, P. Napiorkowski, B. S. Nara Singh, K. Nowak, T. Otsuka, J. Pakarinen, M. Pfeiffer, D. Radeck, P. Reiter, S. Rigby, L. M. Robledo, R. Rodríguez-Guzmán, M. Rudigier, P. Sarriguren, M. Scheck, M. Seidlitz, B. Siebeck, G. Simpson, P. Thöle, T. Thomas, J. Van de Walle, P. Van Duppen, M. Vermeulen, D. Voulot, R. Wadsworth, F. Wenander, K. Wimmer, K. O. Zell, and M. Zielinska, *Phys. Rev. Lett.* **108**, 062701 (2012).
- [11] S. Naimi, G. Audi, D. Beck, K. Blaum, C. Böhm, C. Borgmann, M. Breitenfeldt, S. George, F. Herfurth, A. Herlert, M. Kowalska, S. Kreim, D. Lunney, D. Neidherr, M. Rosenbusch, S. Schwarz, L. Schweikhard, and K. Zuber, *Phys. Rev. Lett.* **105**, 032502 (2010).

- [12] U. Hager, T. Eronen, J. Hakala, A. Jokinen, V. S. Kolhinen, S. Kopecky, I. Moore, A. Nieminen, M. Oinonen, S. Rinta-Antila, J. Szerypo, and J. Äystö, *Phys. Rev. Lett.* **96**, 042504 (2006).
- [13] V. V. Simon, T. Brunner, U. Chowdhury, B. Eberhardt, S. Ettenauer, A. T. Gallant, E. Mané, M. C. Simon, P. Delheij, M. R. Pearson, G. Audi, G. Gwinner, D. Lunney, H. Schatz, and J. Dilling, *Phys. Rev. C* **85**, 064308 (2012).
- [14] H. A. Jahn and E. Teller, *Royal Soc. London Proc. Series A* **161**, 220 (1937).
- [15] P. Cejnar, J. Jolie, and R. F. Casten, *Rev. Mod. Phys.* **82**, 2155 (2010).
- [16] P. Federman and S. Pittel, *Phys. Rev. C* **20**, 820 (1979).
- [17] K. Heyde, J. Jolie, J. Moreau, J. Ryckebusch, M. Waroquier, P. V. Duppen, M. Huyse, and J. Wood, *Nucl. Phys. A* **466**, 189 (1987).
- [18] J. Garcia-Ramos, K. Heyde, R. Fossion, V. Hellemans, and S. De Baerdemacker, *Eur. Phys. J. A* **26**, 221 (2005).
- [19] R. Rodríguez-Guzmán, P. Sarriguren, and L. M. Robledo, *Phys. Rev. C* **82**, 061302(R) (2010).
- [20] R. Rodríguez-Guzmán, P. Sarriguren, L. Robledo, and S. Perez-Martin, *Phys. Lett. B* **691**, 202 (2010).
- [21] E. Chabanat, P. Bonche, P. Haensel, J. Meyer, and R. Schaeffer, *Nucl. Phys. A* **635**, 231 (1998).
- [22] M. Bender, G. F. Bertsch, and P.-H. Heenen, *Phys. Rev. C* **73**, 034322 (2006).
- [23] E. Kugler, *Hyperfine Interact.* **129**, 23 (2000).
- [24] M. Mukherjee, D. Beck, K. Blaum, G. Bollen, J. Dilling, S. George, F. Herfurth, A. Herlert, A. Kellerbauer, H.-J. Kluge, S. Schwarz, L. Schweikhard, and C. Yazidjian, *Eur. Phys. J. A* **35**, 1 (2008).
- [25] S. Kreim, D. Atanasov, D. Beck, K. Blaum, C. Böhm, C. Borgmann, M. Breitenfeldt, T. E. Cocolios, D. Fink, S. George, A. Herlert, A. Kellerbauer, U. Köster, M. Kowalska, D. Lunney, V. Manea, E. Minaya-Ramirez, S. Naimi, D. Neidherr, T. Nicol, R. E. Rossel, M. Rosenbusch, L. Schweikhard, J. Stanja, F. Wienholtz, R. N. Wolf, and K. Zuber, *Nucl. Instrum. Methods Phys. Res. B* (2013), doi: 10.1016/j.nimb.2013.07.072.
- [26] F. Herfurth, J. Dilling, A. Kellerbauer, G. Bollen, S. Henry, H.-J. Kluge, E. Lamour, D. Lunney, R. Moore, C. Scheidenberger, S. Schwarz, G. Sikler, and J. Szerypo, *Nucl. Instrum. Methods Phys. Res. A* **469**, 254 (2001).
- [27] R. Wolf, D. Beck, K. Blaum, C. Böhm, C. Borgmann, M. Breitenfeldt, F. Herfurth, A. Herlert, M. Kowalska, S. Kreim, D. Lunney, S. Naimi, D. Neidherr, M. Rosenbusch, L. Schweikhard, J. Stanja, F. Wienholtz, and K. Zuber, *Nucl. Instrum. Methods Phys. Res. A* **686**, 82 (2012).
- [28] R. Wolf, F. Wienholtz, D. Atanasov, D. Beck, K. Blaum, C. Borgmann, F. Herfurth, M. Kowalska, S. Kreim, Y. A. Litvinov, D. Lunney, V. Manea, D. Neidherr, M. Rosenbusch, L. Schweikhard, J. Stanja, and K. Zuber, *Int. Journ. Mass Spectrom.* **349–350**, 123 (2013).
- [29] H. Raimbault-Hartmann, D. Beck, G. Bollen, M. König, H.-J. Kluge, E. Schark, J. Stein, S. Schwarz, and J. Szerypo, *Nucl. Instrum. Methods Phys. Res. B* **126**, 378 (1997).
- [30] G. Savard, S. Becker, G. Bollen, H.-J. Kluge, R. Moore, T. Otto, L. Schweikhard, H. Stolzenberg, and U. Wiess, *Phys. Lett. A* **158**, 247 (1991).
- [31] G. Gräff, H. Kalinowsky, and J. Traut, *Z. Phys. A: Atoms Nuclei* **297**, 35 (1980).
- [32] M. Wang, G. Audi, A. H. Wapstra, F. G. Kondev, M. MacCormick, X. Xu, and B. Pfeiffer, *Chin. Phys. C* **36**, 1603 (2012).
- [33] R. Iafigliola, H. Dautet, S. W. Xu, J. K. P. Lee, R. Chrien, R. Gill, and M. Shmid, *Proceedings of the 7th International Conference Atomic Masses and Fundamental Constants AMCO-7* (Technische Hochschule Darmstadt, Darmstadt, 1984), p. 141.
- [34] G. Audi, A. Coc, M. Epherre-Rey-Campagnolle, G. L. Scornet, C. Thibault, and F. Touchard, *Nucl. Phys. A* **449**, 491 (1986).
- [35] G. Audi, F. Kondev, M. Wang, B. Pfeiffer, X. Sun, J. Blachot, and M. MacCormick, *Chin. Phys. C* **36**, 1157 (2012).
- [36] S. George, S. Baruah, B. Blank, K. Blaum, M. Breitenfeldt, U. Hager, F. Herfurth, A. Herlert, A. Kellerbauer, H.-J. Kluge, M. Kretzschmar, D. Lunney, R. Savreux, S. Schwarz, L. Schweikhard, and C. Yazidjian, *Phys. Rev. Lett.* **98**, 162501 (2007).
- [37] S. George, K. Blaum, F. Herfurth, A. Herlert, M. Kretzschmar, S. Nagy, S. Schwarz, L. Schweikhard, and C. Yazidjian, *Int. J. Mass Spectrom.* **264**, 110 (2007).
- [38] M. Bender, P.-H. Heenen, and P.-G. Reinhard, *Rev. Mod. Phys.* **75**, 121 (2003).
- [39] N. Schunck, J. Dobaczewski, J. McDonnell, W. Satula, J. Sheikh, A. Staszczak, M. Stoitsov, and P. Toivanen, *Comp. Phys. Commun.* **183**, 166 (2012).
- [40] T. Duguet, P. Bonche, P.-H. Heenen, and J. Meyer, *Phys. Rev. C* **65**, 014310 (2001).
- [41] M. Kretzschmar, *Int. J. Mass Spectrom.* **264**, 122 (2007).
- [42] W. Urban, J. Pinston, J. Genevey, T. Rzaca-Urban, A. Zlomaniec, G. Simpson, J. Durell, W. Phillips, A. Smith, B. Varley, I. Ahmad, and N. Schulz, *Eur. Phys. J. A* **22**, 241 (2004).
- [43] M. Bender, K. Rutz, P.-G. Reinhard, and J. Maruhn, *Eur. Phys. J. A* **8**, 59 (2000).
- [44] P. Delahaye, G. Audi, K. Blaum, F. Carrel, S. George, F. Herfurth, A. Herlert, A. Kellerbauer, H.-J. Kluge, D. Lunney, L. Schweikhard, and C. Yazidjian, *Phys. Rev. C* **74**, 034331 (2006).
- [45] G. Kumbartzki, N. Benczer-Koller, J. Holden, G. Jakob, T. Mertzimekis, M. Taylor, K.-H. Speidel, R. Ernst, A. Stuchbery, C. Beausang, and R. Krücken, *Phys. Lett. B* **562**, 193 (2003).
- [46] P. Federman, S. Pittel, and A. Etchegoyen, *Phys. Lett. B* **140**, 269 (1984).
- [47] P. A. Butler and W. Nazarewicz, *Rev. Mod. Phys.* **68**, 349 (1996).
- [48] O. A. Rosso, W. W. Unkelbach, and G. Molnár, *Nucl. Phys. A* **563**, 74 (1993).
- [49] L. M. Robledo and G. F. Bertsch, *Phys. Rev. C* **84**, 054302 (2011).